EFFECTS OF NON-WKB ALFVÉN WAVES ON A MULTICOMPONENT SOLAR WIND WITH DIFFERENTIAL ION FLOW

Bo Li and Xing Li

Institute of Mathematics and Physics, Aberystwyth University, SY23 3BZ, UK; bbl@aber.ac.uk

ABSTRACT

We present multicomponent solar wind models self-consistently incorporating the contribution from dissipationless, monochromatic, hydromagnetic (with angular frequencies ω well below ion gyrofrequencies), toroidal Alfvén waves, which are coupled to the flow through the wave-induced ponderomotive forces. Protons and alpha particles are treated on an equal footing, and the wavelength is not assumed to be small compared to the spatial scales at which the solar wind parameters vary. We find that the non-WKB effects are significant, for the fast and slow solar wind solutions alike. In comparison with their non-WKB counterparts, the WKB ones are more effective in accelerating the solar wind inside the Alfvén point, producing significantly enhanced ion fluxes and considerably reduced alpha abundance in the inner corona. Only when $\omega \gtrsim 3.5 \times 10^{-3}$ (1.5×10^{-3}) rad s^{-1} can the waves in the fast (slow) winds be adequately described by the WKB limit. Moreover, while the Alfvén waves tend to reduce the magnitude of the proton-alpha speed difference $|U_{\alpha p}|$ in general, different mechanisms operate in two different regimes separated by an $\omega_c \sim$ several $\times 10^{-5}$ rad s^{-1}. This ω_c, defined by equation (15), is closely related to the time required by a solar wind parcel to traverse an Alfvén radius with the speed of center of mass evaluated at the Alfvén point. When $\omega > \omega_c$, the fluctuations are wavelike and tend to accelerate both ion species, thereby losing most of their energy by doing work on ion flows; whereas when $\omega < \omega_c$, a quasi-static behavior results: the fluctuations may act to accelerate the slower flowing ion species but decelerate the faster moving one in a large portion of the computational domain, and only a minor fraction of the wave energy flux injected at the base is lost. The fluctuations with the lowest frequency are no less effective in reducing $|U_{\alpha p}|$ than the WKB waves: in the slow solar wind solutions, they may be able to quench a significant $|U_{\alpha p}|$ with base amplitudes as small as 4 km s^{-1}. The consequences of ω_c on the velocity fluctuation spectra of protons and alpha particles, which are likely to be obtained by future missions like the *Solar Orbiter* and *Solar Probe*, are discussed.

Subject headings: solar wind — stars: winds, outflows — Sun: magnetic fields — waves

1. INTRODUCTION

Alfvén waves have both observational and theoretical consequences in solar wind studies. A salient feature in the measured solar wind fluctuations in interplanetary space (see the reviews by, e.g., Tu & Marsch 1995; Goldstein et al. 1995; Bruno & Carbone 2005), Alfvén waves may as well account for the Faraday rotation measurements inside 10 $R_\odot$ (Hollweg et al. 1982) and the nonthermal broadening of a number of ultraviolet lines measured below ∼5 $R_\odot$ (e.g., Banerjee et al. 1998; Esser et al. 1999). It is noteworthy that although the hourly-scale fluctuations seem to be more frequently studied, the fluctuation spectrum measured by *Helios* nevertheless spans a broad frequency range from 10^{-5} to 10^{-2} s^{-1} (Tu & Marsch 1995). On the theoretical side, it was recognized even before their identification that Alfvén waves may provide a ponderomotive force that accelerates the solar wind (Parker 1965). Furthermore, Alfvén waves may be damped, their energy being converted into both thermal and kinetic energies of the flow. One such damping mechanism that has received much attention is based on the idea that a turbulent cascade toward high parallel wavenumbers transfers the wave energy from the low-frequency hydromagnetic regime to the ion cyclotron one, where the energy can be readily picked up by ions through cyclotron resonance (see the extensive review by Hollweg & Isenberg 2002).

Most solar wind models that incorporate the contribution from Alfvén waves have been formulated in the WKB limit, where the wavelength is assumed to be much shorter than the spatial scale at which the flow parameters vary. On the one hand, this considerably simplifies the mathematical treatment. On the other hand,

some measured features of the solar wind fluctuations do posses a number of WKB characteristics. For instance, the *Helios* measurements revealed that during hourly-scale Alfvénic activities in both the fast and slow wind, protons are heavily perturbed, whereas the velocity of alpha particles suffers little distortion (Marsch et al. 1981, 1982a, 1982b). This discrepancy in the responses of different ion species to Alfvén waves is consistent with the WKB theory, considering that the proton−alpha-particle differential speed is of the order of the local Alfvén speed. In addition, for the extensively studied hourly-scale fluctuations in the fast solar wind around 1 AU, there tends to exist a high correlation between the perturbed magnetic field $\delta \boldsymbol{b}$ and plasma velocity $\delta \boldsymbol{v}$ (Belcher & Davis 1971). As a matter of fact, if examining the normalized cross-helicity spectrum such as given by Figure 2-4 in Tu & Marsch (1995), one may find that the high $\delta \boldsymbol{v}$-$\delta \boldsymbol{b}$ correlation is present across the whole inertial range for fluctuations in the fast solar wind throughout the inner heliosphere explored by *Helios*.

As has long been recognized (Heinemann & Olbert 1980; see also Goldstein et al. 1986), the applicability of the WKB approximation is questionable near the coronal base, where the solar wind is highly inhomogeneous and the phase speed of Alfvén waves is high. There have been several different approaches to assess the finite wavelength effect on Alfvén waves. For instance, Hollweg (1973) extended the WKB analysis to higher order and found that the finite-wavelength correction may lead to a reduction of the wave force below 10 $R_\odot$ for typical solar wind parameters. Another approach was adopted by Heinemann & Olbert (1980), who developed a formalism that is valid for small-amplitude Alfvén

waves with arbitrary frequencies. This formalism has the advantage that outward and inward propagating waves can be explicitly separated, and the coupling between the two can be interpreted as reflection (see also Hollweg & Isenberg 2007). It was shown by Cranmer & van Ballegooijen (2005) that this formalism is essentially equivalent to the form developed by Velli (1993), who expressed the wave transport in terms of the Elsässer variables, and equivalent to the equations derived by Zhou & Matthaeus (1990) if their nonlinear terms are neglected. Note that these nonlinear terms, which are essential for the development of any turbulence, involve the interaction between outward and inward propagating waves. The adoption of Elsässer variables therefore finds application in the one-point closure phenomenology that expresses the damping of the solar wind turbulence, which at least in the case of solar corona is expected to cascade the wave energy toward high perpendicular wavenumbers (e.g., Dmitruk et al. 2001; Cranmer & van Ballegooijen 2005; Verdini et al. 2005; Verdini & Velli 2007). The most recent advance following this direction is the construction of solar wind models that incorporate the contribution of Alfvén waves through both the wave pressure gradient force and turbulent heating (Cranmer et al. 2007).

Nearly all the non-WKB analyses were conducted in the framework of single-fluid magnetohydrodynamics (MHD). In this case, the need to apportion the acceleration and heating among different species is circumvented. However, for the solar wind, alpha particles cannot be regarded as minor, given their nonnegligible abundance and the fact that they may flow considerably faster than protons. In the fast solar wind, the proton-alpha speed difference $U_{\alpha p} = U_\alpha - U_p$ may be up to $\sim$150 km s^{-1} at 0.3 AU, where the proton speed U_p is $\sim$600 km s^{-1} (Marsch et al. 1982a). Moreover, a substantial $U_{\alpha p} \sim 100$ km s^{-1} was also found by *Helios* in the slow solar wind in the presence of Alfvénic fluctuations (Marsch et al. 1981). Consequently, alpha particles can play an important role in determining the evolution of Alfvén waves. So far, the only study that includes alpha particles in a non-WKB analysis for Alfvén waves seems to be that by Li & Li (2007; hereafter Paper I), who demonstrated that substantial deviations exist between the WKB expectation and computed wave properties even for the relatively high angular frequency $\omega = 10^{-3}$ rad s^{-1}. For the purpose of developing the formalism, Paper I examined only the wave propagation in a prescribed low-latitude fast solar wind. However, the computations indicate that the wave acceleration may alter the proton and alpha particle speeds with a wave amplitude as low as 10 km s^{-1} imposed at the coronal base. This is particularly true for the lowest frequency considered, $\omega = 10^{-5}$ rad s^{-1}, in which case the waves may effectively suppress the proton-alpha differential speed in interplanetary space. Therefore, a natural extension to Paper I is to construct solar wind models that self-consistently incorporate the acceleration exerted on ion species by finite-wavelength Alfvén waves. The aim of this paper is to present numerical models thus constructed.

The ponderomotive forces by Alfvén waves may also play a part in determining the helium abundance $n_{\alpha p} = n_\alpha / n_p$ in the inner corona through their influence on the ion flow speeds. It is well established by in situ measurements for regions $r \gtrsim 0.3$ AU that the fast solar wind corresponds to a hardly varying $n_{\alpha p} \sim 4.5\%$, and that in the slow wind $n_{\alpha p}$ is highly variable, ranging from 0.4% to 10% (e.g., McComas et al. 2000). However, $n_{\alpha p}$ in the corona is subject to some controversy, since it has to be indirectly inferred. Concerning the remote-sensing measurements, while evidence exists that $n_{\alpha p}$ may not be enhanced in coronal holes relative to its value for typical fast solar winds (Laming & Feldman 2003), there also exists evidence suggesting the opposite (Delaboudinière 1999). On the other hand, an enhancement in $n_{\alpha p}$ at altitudes of one

or several tenths of solar radius above the limb is nearly inherent to all multifluid models, whether an empirical heating (Hansteen et al. 1997; Lie-Svendsen et al. 2003) or the ion-cyclotron resonance (Li 2003) is applied to generate the solutions. In some cases the corona may even become helium dominated (e.g., Lie-Svendsen et al. 2003). Note that in some models, the bottom boundary is chosen to be in the mid-chromosphere. As a result, the set of governing equations has to be extended to include the neutral components of hydrogen and helium, and the fluxes of both elements in the solar wind show a complex dependence on the processes that happen in the chromosphere and transition region. Neither these processes nor the ion-cyclotron resonance will be considered in the present model, however. Instead, to isolate the non-WKB effects on $n_{\alpha p}$, we will make our model as simple as possible by placing the bottom boundary at the coronal base, and heating the ion species by an empirical energy flux.

The paper is organized as follows. In § 2, we give a brief overview of the equations appropriate for a system consisting of non-WKB Alfvén waves and a multicomponent solar wind flow. Some further details on the numerical implementation of the model are given in § 3. The numerical solutions are then presented in § 4. Finally, § 5 summarizes the results, ending with some concluding remarks.

2. PHYSICAL MODEL

The solar wind model consists of three species, electrons (e), protons (p), and alpha particles (α). Each species s ($s = e, p, \alpha$) is characterized by its density n_s, velocity $\boldsymbol{v}_s$, mass m_s, electric charge e_s, and temperature T_s. The electric charge is also measured in units of electron charge e, i.e., $e_s = Z_s e$ with $Z_e \equiv -1$ by definition. Similarly, the ion mass number A_k follows from the relation $m_k = A_k m_p$ ($k = p, \alpha$). The mass density of species s is $\rho_s = n_s m_s$, and the species partial pressure is $p_s = n_s k_B T_s$, where k_B is the Boltzmann constant. Since the wave frequencies of interest are well below the electron plasma frequency, the condition of quasi-neutrality is guaranteed, $n_e = n_p + Z_\alpha n_\alpha$. Moreover, quasi-zero current is assumed, $\boldsymbol{v}_e = (n_p \boldsymbol{v}_p + Z_\alpha n_\alpha \boldsymbol{v}_\alpha)/n_e$, except when the meridional ion momentum equations are derived.

2.1. *General Description*

Several simplifying assumptions were made in Paper I to facilitate the derivation of the governing equations to be used in this study. For instance, symmetry about the magnetic axis is assumed throughout, i.e., $\partial/\partial\phi \equiv 0$ in the spherical coordinate system (r, θ, ϕ). It is assumed that each species considered can be described by the standard five-moment equations and that the electron inertia can be neglected ($m_e \equiv 0$). The time-varying multicomponent solar wind is then seen as a system where the finite wavelength Alfvén waves are superimposed on an otherwise time-independent flow, with the waves and background flow interacting with each other solely through the wave-induced ponderomotive forces. The effect of solar rotation is neglected. As a result, the unperturbed magnetic field $\boldsymbol{B}_P$ has no ϕ components. Let $\hat{\boldsymbol{e}}_l$ denote the unit vector along $\boldsymbol{B}_P$. A flux-tube coordinate system can then be defined by the base vectors $(\hat{\boldsymbol{e}}_l, \hat{\boldsymbol{e}}_N, \hat{\boldsymbol{e}}_\phi)$ where $\hat{\boldsymbol{e}}_N = \hat{\boldsymbol{e}}_\phi \times \hat{\boldsymbol{e}}_l$ (see Fig. 1). Only purely toroidal Alfvén waves are considered, i.e., the magnetic field $\boldsymbol{B}$ and species velocities $\boldsymbol{v}_s$ ($s = e, p, \alpha$) can be written as

$$\boldsymbol{B} = B_l \hat{\boldsymbol{e}}_l + b \hat{\boldsymbol{e}}_\phi,$$
$$\boldsymbol{v}_s = U_s \hat{\boldsymbol{e}}_l + w_s \hat{\boldsymbol{e}}_N + u_s \hat{\boldsymbol{e}}_\phi, \tag{1}$$
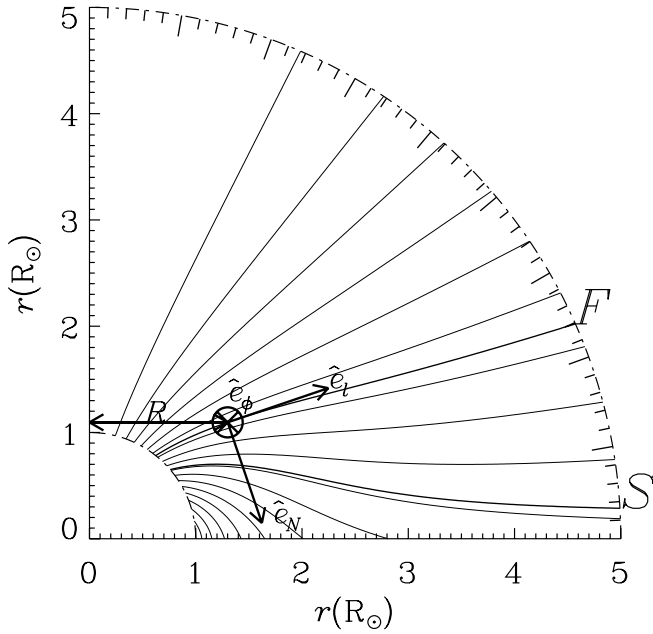
where the lowercase symbols represent perturbations.

FIG. 1.—Adopted meridional magnetic field configuration in the inner corona. Here only a quadrant in which the magnetic axis points upward is shown; thick contours labeled F and S delineate the lines of force along which the fast and slow solar wind solutions are solved for, respectively. Also shown is how to define the geometrical factor R, and the base vectors $\hat{e}_l$, $\hat{e}_N$, and $\hat{e}_\phi$ of the flux tube coordinate system (see § 2.1).

As detailed in Paper I, the mathematical manipulation centers on the fact that for hydromagnetic waves, ω is many orders of magnitude lower than the ion gyrofrequency $\Omega_k = (Z_k e B_l)/(m_k c)$ $(k = p, \alpha)$, where c denotes the speed of light. As a consequence, the ion velocity difference vector has to be aligned with the instantaneous magnetic field. Combined with the assumption of quasi-zero current, this leads to

$$u_k = u_e + \frac{b}{B_l}(U_k - U_e) \qquad (2)$$

where $k = p, \alpha$. Moreover, the velocity perturbations w_s ($s = e, p, \alpha$) are so small that the mass and energy exchange between adjacent magnetic flux tubes can be safely neglected. One needs to retain w_s only in the simplified ion momentum equations to ensure the conservation of total momentum. In other words, the system of vector equations is allowed to be expressed as a force balance condition across the meridional magnetic field, together with a set of transport equations along it. For simplicity, in the present study the force balance condition is replaced by prescribing a meridional magnetic field to be detailed in § 3.1, and only the equations governing the time-independent multicomponent flow and the transport of Alfvén waves are considered. In essence, this is a one-dimensional model in that there is only one independent spatial variable, l, the arc length along a given magnetic line of force measured from its footpoint at the solar surface.

2.2. Equations Governing the Wave Transport

The equations governing the transport of Alfvén waves in a multicomponent solar wind are the ϕ components of the magnetic induction law and the total momentum conservation (eqs. [12] and [16] in Paper I). Using the total momentum as opposed to individual momenta of ion species is necessary to eliminate the terms associated with ion gyrofrequencies. The analysis of the two equations can then be considerably simplified with the in-

troduction of the Fourier amplitudes at a given angular frequency ω, i.e.,

$$[b(l, t), u_s(l, t)] = [\tilde{b}(l), \tilde{u}_s(l)] \exp(-i\omega t), \qquad (3)$$

where $s = e, p, \alpha$. Further introducing two dimensionless variables

$$\xi = \tilde{b}/B_l, \quad \eta = \tilde{u}_e/U_A, \qquad (4)$$

where $U_A = B_l/(4\pi\rho)^{1/2}$ is the Alfvén speed determined by the total mass density $\rho = \rho_p + \rho_\alpha$, Paper I yields that the perturbations obey

$$(M_T^2 - 1)\xi' = F_{11}\xi + F_{12}\eta, \qquad (5a)$$

$$(M_T^2 - 1)\eta' = F_{21}\xi + F_{22}\eta. \qquad (5b)$$

By doing so, the original partial differential equations are reduced to two ordinary ones, which involve only the directional differentiation along the poloidal magnetic field $\partial/\partial l$, denoted by the prime $'$ for brevity. In addition, the combined meridional Alfvénic Mach number M_T is defined by

$$M_T^2 = 4\pi(\rho_p U_p^2 + \rho_\alpha U_\alpha^2)/B_l^2. \qquad (6)$$

The expressions for the complex-valued coefficients F_{11}, F_{12}, F_{21} and F_{22}, given by equations (40a) to (40d) in Paper I, involve the flow parameters ρ_k and U_k ($k = p, \alpha$), the meridional magnetic field B_l, as well as ω. Obviously, equation (5) possesses an apparent singularity at the Alfvén point where $M_T = 1$, which lies between 1 $R_\odot$ and 1 AU for typical solar winds.

Given a line of force and the background flow parameters, equation (5) may be solved for the Fourier amplitudes for the electron velocity and the magnetic field perturbations if ω is also known. The ion velocity perturbations are then found from the alignment condition (2). By assumption, the feedback from waves to the solar wind flow is through the wave-induced acceleration a_k ($k = p, \alpha$) given by

$$a_k = \langle u_k^2 \rangle (\ln R)' - \frac{Z_k}{4\pi n_e m_k} \left\langle b \frac{\partial b}{\partial l} + b^2 (\ln R)' \right\rangle - \frac{\langle b X_k \rangle}{B_l}, \quad (7)$$

where the angular brackets represent the time-average over one wave period, which can be readily evaluated using the Fourier amplitudes (cf. eq. [21] in Paper I). In addition, $R = r \sin \theta$ is a geometrical factor evaluated at each point along the meridional magnetic field line (see Fig. 1). The variable X_k is defined by $X_k = \Omega_k(w_j - w_k)(Z_j n_j/n_e)$, where j stands for the ion species other than k, i.e., $j = \alpha$ for $k = p$ and vice versa.

Due to the presence of w_k in X_k, one might expect that the N-component of the ion momentum equations has to be solved. In fact, there is no need to do so, because X_k involves only the difference $w_j - w_k$ and may be determined immediately after u_k and b are found,

$$X_k = \frac{\partial u_k}{\partial t} + U_k \left[\frac{\partial u_k}{\partial l} + u_k (\ln R)' \right]$$
$$- \frac{Z_k}{4\pi n_e m_k} B_l \left[\frac{\partial b}{\partial l} + b (\ln R)' \right]. \qquad (8)$$

The algebraic manipulation leading to this rather interesting behavior was first devised by McKenzie et al. (1979) when deriving the expressions for the force introduced into the meridional ion momentum equation by solar rotation. McKenzie et al. (1979)

TABLE 1
Parameters Used to Generate Solar Wind Solutions

	Magnetic Field θ_E (deg)	Heat Deposition			Base Flow Parameters		
Wind Type		F_E (erg cm^{-2} s^{-1})	l_d ($R_\odot$)	χ	T_b (10^6 K)	$n_{e,b}$ (10^8 cm^{-3})	$(n_\alpha/n_p)_b$ (%)
Fast............................	70	1.7	1.6	1.7	1	3	6
Slow	89	1.2	1.4	4	1.4	3	6

noted that this practice is in effect an expansion in terms of a small parameter $\Omega_\odot/\Omega_k$, where $\Omega_\odot$ is the angular rotation rate of the Sun. That the technique also applies when hydromagnetic Alfvén waves are concerned is not surprising, given that the Alfvén waves in this study are represented by the azimuthal twists and there also exists a small parameter ω/Ω_k.

Equation (5) is analytically tractable in the WKB limit where ω is sufficiently high to ensure that the background flow parameters vary little within one wavelength. To the lowest order, the WKB approximation yields that $\langle b^2 \rangle$ satisfies the equation

$$\langle b^2 \rangle \frac{\rho(U_{\rm ph} - U_m)U_{\rm ph}^2}{B_l^3} = {\rm const}, \qquad (9)$$

where $U_m = (\rho_p U_p + \rho_\alpha U_\alpha)/\rho$ is the speed of center of mass, while the phase speed $U_{\rm ph}$ is given by the dispersion relation

$$\sum_k \rho_k(U_{\rm ph} - U_k)^2 = \frac{B_l^2}{4\pi}, \qquad (10)$$

with $k = p, \alpha$. Furthermore, the amplitudes of the species velocity and magnetic field fluctuations are related by

$$|u_s| = (U_{\rm ph} - U_s)\frac{|b|}{B_l}, \qquad (11)$$

where $s = e, p, \alpha$. Finally, a compact expression is found for the wave acceleration a_k,

$$a_k = \left(\frac{U_{\rm ph}^2 - U_k^2}{2B_l^2}\langle b^2 \rangle\right)'. \qquad (12)$$

2.3. Equations Governing the Time-independent Solar Wind

From Paper I, the equation governing the meridional speed of ion species k reads

$$U_k U_k' = -\frac{p_k'}{n_k m_k} - \frac{Z_k p_e'}{n_e m_k} - \frac{GM_\odot}{r}(\ln r)'$$
$$+ \frac{n_j}{A_k n_e} c_0(U_j - U_k) + a_k, \qquad (13)$$

where $k = p, \alpha$. The gravitational constant is denoted by G, and $M_\odot$ is the mass of the Sun. In addition, c_0 is a coefficient associated with Coulomb frictions, which unsurprisingly also involve the ion species j other than k. We take the Coulomb logarithm to be 21 when evaluating c_0 via the expression given in the Appendix of Li & Li (2006). Other equations concern the mass conservation for both ion species $k = p, \alpha$, and energy transport for all the species $s = e, p, \alpha$. For simplicity, the ion heat fluxes are neglected, and the Spitzer law for the electron heat flux q_e is assumed, $q_e = -\kappa T_e^{5/2} T_e'$, where $\kappa = 7.8 \times 10^{-7}$ erg K$^{-7/2}$ cm^{-1} s^{-1} (Spitzer 1962).

If the wave acceleration a_k is a known function of l, the model equations can be solved for the distributions along a given magnetic line of force of the densities n_k and meridional speed U_k of ion species ($k = p, \alpha$) as well as the temperatures T_s of all species ($s = e, p, \alpha$). However, a_k is not known a priori, but rather depends on the flow parameters themselves, thereby coupling the waves and solar wind flow. Further complication comes from the finite wavelength effect, which introduces an apparent singularity at the Alfvén point where $M_T = 1$ for the wave equation (5). The numerical method employed for solving such an involved system of equations is described in the next section.

3. NUMERICAL IMPLEMENTATION

It is necessary to solve the governing equations described in § 3 numerically for a quantitative analysis to be made. To this end, the meridional magnetic field configuration should be prescribed, some external heat deposition needs to be applied to ions to generate the solar wind solutions, and appropriate boundary conditions need to be supplemented for both the wave and flow equations. The implementation of these issues and a description of the method of solution are given in this section.

3.1. Background Meridional Magnetic Field

For the meridional magnetic field, we adopt an analytical model given by Banaszkiewicz et al. (1998). In a spherical coordinate system, their equation (5b) can be rewritten as

$$\psi(r, \theta) = M\left[\frac{\sin^2 \theta}{r} + \frac{3Q}{8}\frac{\sin^2 \theta}{r^3}(4 - 5\sin^2 \theta)\right.$$
$$\left. + \frac{K}{a_1}\left(1 - \frac{a_1 + r|\cos \theta|}{\sqrt{r^2 + a_1^2 + 2a_1 r|\cos \theta|}}\right)\right],$$

where ψ denotes the magnetic flux function, whose contours delineate the magnetic lines of force. The poloidal magnetic field is then given by

$$[B_r, B_\theta] = \frac{1}{r\sin\theta}\left[\frac{1}{r}\frac{\partial\psi}{\partial\theta}, -\frac{\partial\psi}{\partial r}\right].$$

In the present implementation, the model magnetic field consists of the dipole and current-sheet components only. A set of parameters $M = 2.9687$, $Q = 0$, $K = 0.9343$, and $a_1 = 1.5$ are chosen such that the last open magnetic field line is anchored at heliocentric colatitude $\theta = 50°$ on the Sun, while at the Earth orbit, the meridional magnetic field strength B_l is 4γ and independent of colatitude θ, consistent with *Ulysses* measurements (Smith & Balogh 1995).

The background magnetic field configuration is depicted in Figure 1, where the thick contours labeled F and S represent the lines of force along which we solve for fast and slow solar wind solutions, respectively. They are also distinguished by the colatitudes θ_E where they reach the Earth orbit $r_E = 1$ AU in Table 1, which summarizes the parameters employed to generate

the solar wind solutions. Tube F (S), which intersects the Earth orbit at $70°$ ($89°$) colatitude, originates from $\theta = 38.5°$ ($49.4°$) at the Sun, where the meridional magnetic field strength B_l is 5.24 (4.66) G.

3.2. Ion Heating

The external energy deposition is assumed to come from an ad hoc energy flux that dissipates at a constant length l_d. The resulting total heating rate is therefore

$$Q = F_E \frac{B_l}{B_{l,E} l_d} \exp\left(-\frac{l}{l_d}\right),$$

where F_E is the input flux scaled to the Earth orbit $r_E = 1$ AU, and $B_{l,E}$ is the meridional magnetic field strength at r_E. The heating rate Q is then apportioned between protons and alpha particles according to

$$Q_p + Q_\alpha = Q, \quad \frac{Q_\alpha}{Q_p} = \frac{\chi \rho_\alpha}{\rho_p}, \quad (14)$$

where χ is a constant that indicates how alpha particles are favored when Q is distributed, with $\chi = 1$ standing for the neutral heating; the total energy that goes to ion species k is proportional to its mass density ρ_k ($k = p, \alpha$). The choice of the heat deposition needs some explanation. An exponential form of Q was first suggested by Holzer & Axford (1970) and was later employed in a large number of studies. The form of Q adopted here is slightly different from the original version to ensure that it mimics the dissipation of a flux of nonthermal energy. The way the dissipated energy is distributed resembles the mechanism involving ion-cyclotron waves (cf. Isenberg & Hollweg 1983; Hu & Habbal 1999). Previous computations invoking such mechanisms indicate that, in the case of neutral heating, alpha particles tend to flow more slowly than protons (see the dispersionless case in Fig. 1 of Hu & Habbal 1999). Only when alpha particles are energetically favored in the corona can the modeled $U_{\alpha p}$ be positive in interplanetary space. This happens when $\chi > 1$. Listed in Table 1, the heating parameters are chosen to yield fast and slow solar wind solutions with realistic ion mass fluxes and terminal speeds in the absence of wave contribution. As a result, the influence introduced by the non-WKB Alfvén waves can be deduced.

3.3. Boundary Conditions and Method of Solution

The governing equations consisting of the flow part (eqs. [8]–[10] in Paper I) and the wave part (eq. [38] in Paper I) are solved on a spatial grid extending from the coronal base (1 $R_\odot$) out to 100 $R_\odot$. Both parts need to be supplemented with appropriate boundary conditions. For the flow part, at the base 1 $R_\odot$ the flow speeds U_p and U_α are determined by mass conservation, whereas the ion densities as well as species temperatures are fixed. These parameters are given in Table 1, where the ion densities are given in terms of the base values of the electron density $n_{e,b}$ and the alpha particle abundance $(n_\alpha/n_p)_b$. At the top boundary (100 $R_\odot$), all the flow parameters are linearly extrapolated for simplicity. On the other hand, for a monochromatic wave with angular frequency ω, the regularity requirement at the Alfvén point means that the wave acceleration a_k is determined only by one parameter, which is chosen to be the electron velocity fluctuation amplitude $\langle u_e^2 \rangle^{1/2}$ at 1 $R_\odot$, or δu_b for brevity. To evaluate the non-WKB effect, we also construct models with WKB waves with the same base flow conditions and identical base wave amplitudes.

We adopt an iterative approach to simultaneously solve the nonlinear system of equations. With an initial guess for the flow parameters, the wave acceleration a_k ($k = p, \alpha$) can be obtained as follows. When a non-WKB Alfvén wave with a given ω is considered, equation (5) is first solved analytically at the Alfvén point, and then integrated both inward to the coronal base and outward to 100 $R_\odot$ using the standard fourth-order Runge-Kutta method. One can find a_k through equation (7). When constructing models with WKB waves, the amplitude of the magnetic field fluctuation $|b|$ is first found at the base from relation (11), and then computed via equation (9) for the whole computational domain. The wave acceleration a_k is readily obtained from equation (12). The flow equations (eqs. [8] to [10] in Paper I) incorporating a_k are then solved by using the numerical scheme devised by Hu et al. (1997), and thereby all the flow parameters are updated. To ensure internal consistency, the two steps are iterated until a convergence is met. This iterative approach closely follows those used by Alazraki & Couturier (1971) and MacGregor & Charbonneau (1994), where WKB and non-WKB Alfvén waves are self-consistently included in single-fluid solar wind models, respectively.

4. NUMERICAL RESULTS

Having described the solution method, we are now in a position to answer the following questions: to what extent are the wind parameters affected by the non-WKB effect in general? and how are the helium abundance and the proton–alpha particle differential speed affected in particular? To address these questions, we will only vary those parameters characterizing the waves, namely, the base wave amplitude δu_b and angular frequency ω. There has been considerable effort made to determine ξ, the nonthermal motions that contribute to the broadening of some UV lines, in the solar upper atmosphere by using SUMER and UVCS data (e.g., Banerjee et al. 1998; Chae et al. 1998; Peter 1999; Esser et al. 1999). Typically ξ is found to be $\sim$30 km s^{-1} at an altitude of $\sim$0.02 $R_\odot$ above limb. Since this value corresponds to the line-of-sight component, the overall magnitude of the nonthermal motion may be $\sqrt{2}\xi$ for circularly polarized waves (cf. Banerjee et al. 1998; Cranmer & van Ballegooijen 2005). Given that the waves examined here are linearly polarized, δu_b will be allowed to have a value of up to 40 km s^{-1}. In this section, we will fist examine the fast and then the slow solar wind.

4.1. Fast Solar Wind Solutions

Figure 2 examines the flow properties of the fast solar wind solutions corresponding to several ω as plotted by different line styles indicated in Figure 2a. For comparison, also displayed are the solution incorporating WKB waves (dash-dotted curves) and that without wave contribution (long-dashed curves; only shown in the right column). The models involving waves all pertain to a wave amplitude of $\delta u_b = 28$ km s^{-1}. The left column gives the radial distributions near the base of the flow $r \leq 2 R_\odot$ of the flow speeds of (a) protons U_p and (b) alpha particles U_α, as well as that of (c) the alpha particle abundance $n_{\alpha p} = n_\alpha/n_p$. In addition, the right column gives the radial profiles for the entire computational domain of (d) U_p, (e) U_α, and (g) the difference between the two, $U_{\alpha p} = U_\alpha - U_p$. The asterisks in the right column mark the Alfvén point, where the combined meridional Alfvénic Mach number $M_T = 1$, with M_T defined by equation (6). Moreover, for the solutions with waves the diamonds correspond to the location r_{NL} where the amplitude of the wave-induced magnetic field fluctuations equals the background, i.e., $\langle b^2 \rangle / B_l^2 = 1$. Care has to be taken when one examines the segments at distances beyond those diamonds, since when deriving the wave equation (5), we assume that the time-dependent solar wind flow may be decomposed into
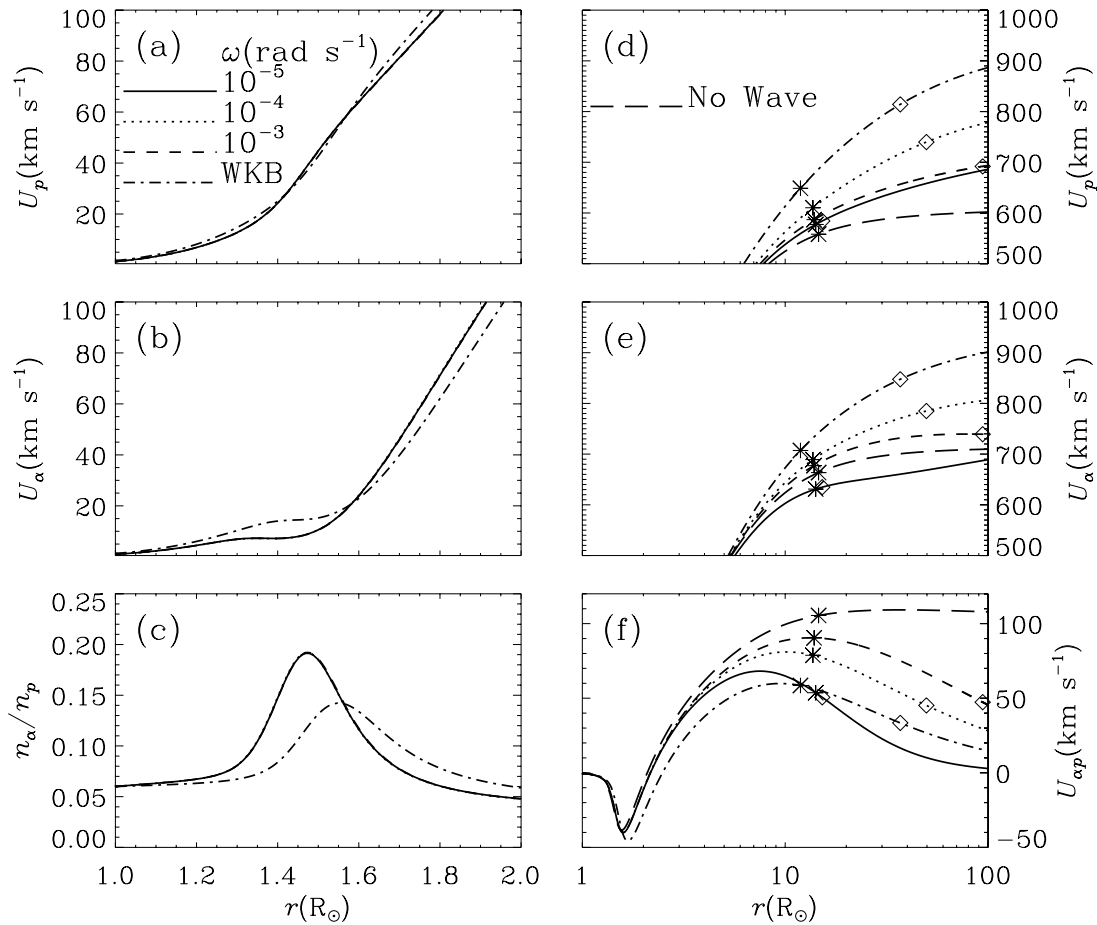
Fig. 2.—Multicomponent solar wind models incorporating non-WKB Alfvén waves. Numerical results for three angular frequencies and for the WKB wind model are given in different line styles, as indicated in (a). All models have the same base velocity fluctuation amplitude $\delta u_b = 28$ km s^{-1}. Radial profiles are shown for: (a and d) the proton flow speed U_p, (b and e) the alpha flow speed U_α, (c) the alpha abundance n_α/n_p, and (f) the proton-alpha differential speed $U_{\alpha p} = U_\alpha - U_p$. Panels in the left column give a close-up of the inner corona $r \leq 2\,R_\odot$. In (d), (e), and (f), the long-dashed curves correspond to the waveless model, and the asterisks indicate the location of the Alfvénic point, defined by eq. (6) to be the location where the combined Alfvénic Mach number $M_T = 1$. The diamonds mark the location where the wave-induced magnetic field fluctuation amplitude starts to exceed the background.

a steady background and Alfvén waves. One might expect that when the wave amplitudes are significant, such a decomposition is not permitted. However, as first discussed by Lou (1993), the source terms introduced into the momentum and magnetic induction equations by wave-induced fluctuations decrease asymptotically sufficiently rapidly with distance. Consequently, the first-order wave amplitudes are valid provided that the wave amplitude imposed at the coronal base is sufficiently small. Nevertheless, the portions where $\langle b^2 \rangle / B_l^2 \geq 1$ are indicated for clarity, and we have excluded all solutions for which $r_{NL} < r_A$ so that integrating the wave equation backward from r_A to the coronal base is formally allowed.

A close examination of the left column of Figure 2 reveals that the non-WKB models are virtually indistinguishable. Actually, they differ only slightly from the waveless model, indicating that the wave acceleration associated with these frequencies plays an insignificant role in the force balance for protons or alpha particles in the region considered. On the other hand, an obvious difference exists between the WKB and non-WKB wind models. For instance, Figures 2a and 2b demonstrate that the WKB model tends to produce a higher flow speed for both protons and alpha particles near the base, and hence a higher ion flux as the ion densities are fixed at 1 $R_\odot$. Consider the proton and alpha fluxes scaled to 1 AU, $(n_p U_p)_E$ and $(n_\alpha U_\alpha)_E$. In the WKB case $(n_p U_p)_E$ [$(n_\alpha U_\alpha)_E$] is 3.18×10^8 [1.49×10^7] cm^2 s^{-1}, whereas in the model with

$\omega = 10^{-5}$ rad s^{-1}, $(n_p U_p)_E$ and $(n_\alpha U_\alpha)_E$ are 2.6×10^8 and 1.14×10^7 cm^2 s^{-1}, respectively. Furthermore, as shown in Figure 2c, the WKB case corresponds to a reduced alpha abundance $n_{\alpha p}$ for $r \lesssim 1.56\,R_\odot$, with the local maximum $n_{\alpha p, M}$ decreasing from 0.19 attained at $1.47\,R_\odot$ in the non-WKB models to 0.14 at $1.55\,R_\odot$ in the WKB one. This change may be readily understood, since compared with their non-WKB counterparts, the WKB waves produce an enhancement of the alpha speed U_α larger than the proton one, U_p. As a result, at the base of the wind the WKB model yields a smaller U_p/U_α and hence a smaller n_α/n_p, since the ion flux ratio $(n_\alpha U_\alpha)/(n_p U_p)$ is a constant for steady flows. An interesting aspect of Figure 2b is that the alpha flow speed U_α in the WKB model becomes smaller than in the non-WKB models for $r \gtrsim 1.58\,R_\odot$, despite the fact that the WKB wave acceleration exerted on alpha particles $a_{w,\alpha}$ is substantially larger than the non-WKB throughout the region considered (see Fig. 3b). This is because close to the coronal base, the reduced alpha abundance n_α/n_p in the WKB model gives rise to a lower heating rate for alpha particles (cf. eq. [14]) and therefore a lower alpha temperature. Hence, the lowered alpha pressure gradient force results in a U_α profile that is less steep at $r \gtrsim 1.42\,R_\odot$.

Now turn to the right column of Figure 2, from which one may gain a first impression of the overall influence introduced by the non-WKB effect on the flow parameters. Take the variation of the location of the Alfvén point, r_A, for example. For $\omega = 10^{-5}$,
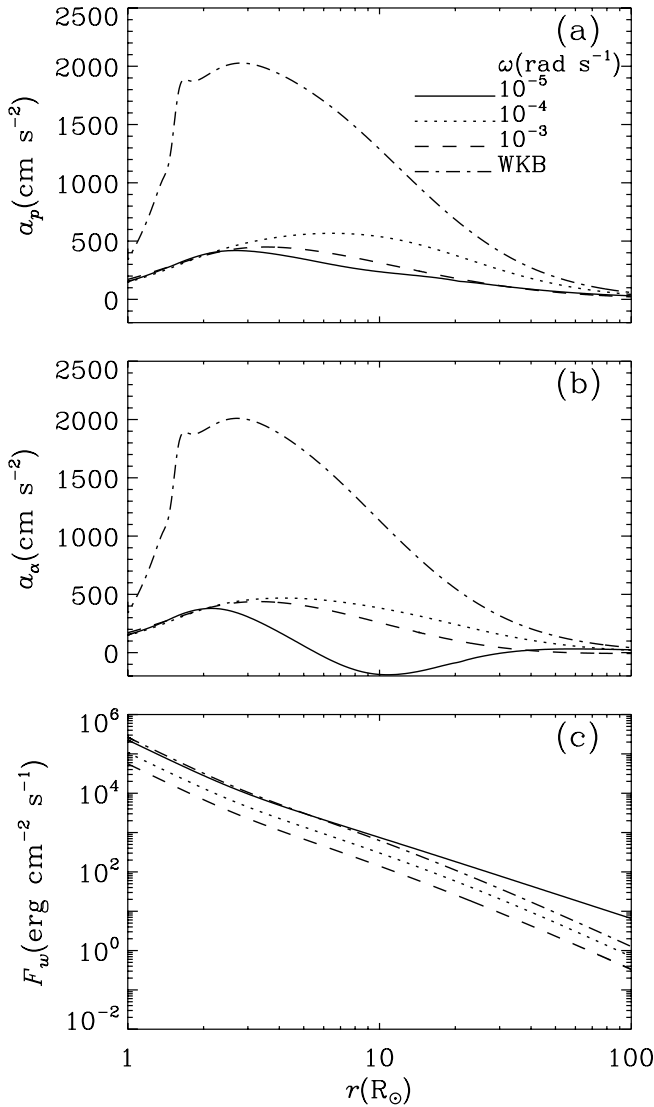
Fig. 3.—Properties of non-WKB Alfvén waves in self-consistently constructed multicomponent solar wind models. Shown are the radial distributions of the wave acceleration experienced by (a) protons and (b) alpha particles, as well as (c) the wave energy flux density for three angular frequencies and the WKB wind model as given by different line styles indicated in (a). All models have a common base velocity fluctuation amplitude $\delta u_b = 28$ km s^{-1}.

10^{-4}, and 10^{-3} rad s^{-1}, r_A is 14, 13.6, and 13.9 $R_\odot$, respectively. These values are close to $r_A = 14.6\,R_\odot$ derived for the waveless model. On the other hand, r_A is 11.9 $R_\odot$ in the WKB model, reinforcing the fact that the WKB Alfvén waves are more effective than the non-WKB ones in accelerating the solar wind flow in the sub-Alfvénic portion. However, Figure 2d indicates that even in the WKB case, the proton speed U_p is only 648 km s^{-1} at r_A, which is only slightly enhanced compared with the model without waves, for which $U_p = 577$ km s^{-1} at the Alfvén point. More significant difference arises in the super-Alfvénic portion, where protons receive a continuous acceleration from both the WKB and non-WKB Alfvén waves. Furthermore, the proton flow speed does not show a monotonic dependence on wave frequency. For instance, at 100 $R_\odot$, the WKB wind model yields a $U_p = 887$ km s^{-1}, whereas the non-WKB models yield $U_p = 686$, 778, and 694 km s^{-1} for $\omega = 10^{-5}$, 10^{-4}, and 10^{-3} rad s^{-1}, respectively. For comparison, the waveless model obtains 602 km s^{-1} for U_p at the same location.

Inspection of Figure 2e shows that among the non-WKB models considered, the one with $\omega = 10^{-5}$ rad s^{-1} shows a fundamental difference from the rest as far as the alpha flow speed U_α is concerned: this wave tends to decelerate rather than accelerate the alpha particles. In fact, for the entire computational domain U_α is even smaller than that in the waveless model. In contrast, similar to the WKB case, the non-WKB models with $\omega = 10^{-4}$ and 10^{-3} rad s^{-1} produce a higher U_α compared with the model without waves. The disparate effects on the ion flows of fluctuations with $\omega = 10^{-4}$ and 10^{-5} rad s^{-1} signify a transition around some ω_c below which the waves behave in a quasi-static manner, a feature extensively discussed by Heinemann & Olbert (1980) and Lou (1993) in the case of single-fluid MHD. Given a background flow, ω_c in the present case can be approximated by

$$\omega_c \approx U_{mA}/(2r_A), \qquad (15)$$

where U_{mA} is the speed of the center of mass evaluated at the Alfvén point. Note that when the non-WKB waves are self-consistently incorporated, the right-hand side of equation (15) may depend on the wave frequency and base amplitude. However, it turns out that the dependence is rather weak; a value of $\omega_c \sim 3 \times 10^{-5}$ rad s^{-1} applies for all the fast solar wind solutions considered. For those $\omega > \omega_c$, one may expect that the waves will be increasingly WKB-like with increasing ω, whereas for $\omega < \omega_c$, the effects of quasi-static fluctuations are similar to those of solar rotation, the zero-frequency solution to the wave equation.

Whether or not a quasi-static behavior results, the net effect of Alfvén waves on the speed difference $U_{\alpha p}$ is to reduce its magnitude, as evidenced by Figure 2f. For instance, for $\omega = 10^{-5}$ rad s^{-1} one finds that $U_{\alpha p} =$ is 2.87 km s^{-1} at 100 $R_\odot$, where the corresponding values for $\omega = 10^{-4}$ and 10^{-3} rad s^{-1} are 28.2 and 45.5 km s^{-1}, respectively. As for the WKB model, one finds that $U_{\alpha p} = 14.7$ km s^{-1}. All these values are considerably smaller than 108 km s^{-1}, found at the same location in the waveless model. This is not surprising, since it is readily shown that if the flow speeds are entirely determined by the wave forces, then

$$\left(U_\alpha^2 - U_p^2\right)\left(1 + \epsilon \frac{\langle b^2 \rangle}{B_l^2}\right) = \text{const}, \qquad (16)$$

where the factor $\epsilon = 1$ for WKB waves. On the other hand, relation (16) also holds when ω approaches zero (cf. Li & Li 2006); the only difference is that ϵ should be chosen to be 2. For a wave with an arbitrary finite ω, it is natural to expect that the effect lies between the two extremes. Now that the ratio $\langle b^2 \rangle/B_l^2$ increases monotonically with increasing r for all the wave models considered, all models should yield a $U_{\alpha p}$ decreasing with r if $U_\alpha + U_p$ does not show a substantial variation, as confirmed by the super-Alfvénic portions of the flow.

The behavior of the flow parameters is further explained by Figure 3, which displays the radial profiles of the wave acceleration inflicted on (a) protons a_p and (b) alpha particles a_α, as well as (c) the wave energy flux density F_w. Numerical results are shown for the three angular frequencies considered, and the WKB model. Figures 3a and 3b show that within $\sim 2\,R_\odot$ the non-WKB wave accelerations differ little from one another, but are considerably smaller than that in the WKB case. Specifically, one finds that at 2 $R_\odot$, for $\omega = 10^{-5}$, 10^{-4}, and 10^{-3} rad s^{-1}, a_p is 384, 375, and 373 cm s^{-2}, respectively, while the WKB model yields a value of 1904 cm s^{-2}. At larger distances, the difference between the WKB and non-WKB models is also prominent. For instance, at 100 $R_\odot$, one finds that $a_p = 58.9$ cm s^{-2} for the WKB model,

while 30.2, 42.7, and 21.7 cm s^{-2} for $\omega = 10^{-5}$, 10^{-4}, and 10^{-3} rad s^{-1}, respectively. The nonmonotonic frequency dependence of a_p is the direct reason for the similar dependence of the proton speed U_p. Likewise, the reduction of the alpha speed U_α for $\omega = 10^{-5}$ rad s^{-1} relative to the waveless model results from the fact that in a large portion of the computational domain, $5.7 \lesssim r/R_\odot \lesssim 31.1$ to be precise, the wave exerts a negative a_α on alpha particles. For $\omega = 10^{-3}$ and 10^{-4} rad s^{-1}, however, the waves tend to accelerate the alpha particles, as in the WKB case. Note that in relation (16), the wave effect in limiting $|U_{\alpha p}|$ does not rely on the sign of $U_{\alpha p}$. Hence, we may conclude that the reduction of $|U_{\alpha p}|$ is achieved in different manners by wavelike and quasi-static fluctuations. While wavelike fluctuations tend to provide overall acceleration for both ion species, the quasi-static ones may accelerate the slower flowing species but decelerate the species that flows faster. It is noted, however, that the conclusion is based on the condition that $|U_{\alpha p}| \lesssim U_A$, which holds for both the fast and slow solar wind as measured by *Helios* (Marsch et al. 1982a), and is also true for all the wave-based solutions examined here. For $|U_{\alpha p}| \gtrsim U_A$, kinetic instabilities may arise when the proton beta is comparable to unity and the physics is more complicated (e.g., Gary et al. 2000). If $|U_{\alpha p}|$ is larger still, then from equation (10) one may deduce that a low-frequency electromagnetic Alfvén instability will set in (cf. Verheest 1977). Both subjects are beyond the scope of the present paper.

To proceed, we note that the governing equations allow an energy conservation law to be derived, from which it is readily recognized that at large distances $r \gg r_A$, the gain in the ion kinetic and gravitational potential energy fluxes derives primarily from the energy fluxes associated with waves and the adopted ion heating. In other words, by noting that at $r \gg r_A$ the empirical energy flux has been exhausted, one may deduce the overall contribution of Alfvén waves between 1 $R_\odot$ and r from the relation

$$\sum_{k=p,\alpha} \left(\frac{\rho_k U_k B_{l,\mathrm{E}}}{B_l} \right) \frac{U_k^2(r) + V_{\mathrm{esc}}^2}{2} \approx W(R_\odot) - W(r) + F_{\mathrm{E}}, \quad (17)$$

where $W = (B_{l,\mathrm{E}}/B_l)F_w$ denotes the wave energy flux scaled to the Earth orbit, and $V_{\mathrm{esc}} = (2GM_\odot/R_\odot)^{1/2}$ is the escape speed. Equation (17) indicates that if the ion fluxes in different models are similar, then the asymptotic ion speed U_k is largely determined by the difference of W between 1 $R_\odot$ and r, which hereafter will be taken as 100 $R_\odot$. Moreover, at large distances U_α is close to U_p in models with waves. Therefore, a frequency dependence of ΔW similar to that of U_p is expected, and indeed is reproduced in Figure 3c. For instance, $\Delta W = W(R_\odot) - W(100\,R_\odot)$ is found to be 0.31, 0.67, and 0.36 (here and hereafter in units of erg cm^{-2} s^{-1}) for $\omega = 10^{-5}$, 10^{-4}, and 10^{-3} rad s^{-1}, respectively. On the other hand, $\Delta W = 1.75$ is considerably larger in the WKB model. In fact, this value more than compensates for the enhancement of the ion speeds in that among the examined ion fluxes the WKB model also yields the largest value. An interesting feature is that unlike the frequency dependence of ΔW, at 1 $R_\odot$ the wave energy flux density for $\omega = 10^{-5}$ rad s^{-1} is the closest to the corresponding WKB value. Specifically, when scaled to R_{E}, the WKB model yields $W(R_\odot) = 2.02$, whereas the values for $W(R_\odot)$ are 1.73, 0.82, and 0.43 for $\omega = 10^{-5}$, 10^{-4}, and 10^{-3} rad s^{-1}, respectively. From the definition of the wave energy flux density (cf. eq. [20b] in Paper I), it is easily understood that this feature comes largely from the frequency dependence of the wave-induced magnetic fluctuation b. For $\omega = 10^{-5}$, 10^{-4}, 10^{-3}, and the WKB model, $|b|$ is found to be 0.28, 0.15, 0.082, and 0.32 G, respectively. Now examine the fraction $\Delta W/W(R_\odot)$. One can see that

only 18.1% of the injected wave flux is lost in the form of the work done on the ion flows for $\omega = 10^{-5}$ rad s^{-1}, whereas for the WKB model the corresponding fraction is 86.4%. As for the model with $\omega = 10^{-4}$ (10^{-3}) rad s^{-1}, this fraction is 81.4% (83.2%), close to that found in the WKB case. Therefore, one may envision that ω_c also distinguishes fluctuations in their efficiency of losing energy to the solar wind flow, with the quasi-static ones being much less efficient.

One may have noticed that in the cases with $\omega = 10^{-3}$ and $\omega = 10^{-4}$, as well as in the WKB model, the F_w profiles are rather similar. As has been discussed in Paper I, in the near-Sun regions the F_w profiles for all the examined waves roughly behave like $F_w \propto B_l$, indicating that the wave energy is diluted only by the expansion of the magnetic flux tube. On the other hand, at large distances $r \gg r_A$, the F_w profiles for $\omega = 10^{-3}$ and 10^{-4} rad s^{-1} roughly comply with the WKB expectation, i.e., $F_w \sim r^{-3}$, since in the region considered the WKB limit applies in these two cases. When it comes to the model where $\omega = 10^{-5}$ rad s^{-1}, one may find that asymptotically $F_w \sim r^{-2}$, approximately.

Figure 4 expands the obtained results by displaying the dependence on the angular frequency ω of some flow parameters for waves with four different base amplitudes, $\delta u_b = 4, 16, 28,$ and 40 km s^{-1}. For comparison, the waveless model is shown by the dashed lines, while the corresponding WKB results are given by the horizontal bars at the right of each panel. Plotted in Figure 4 are (a) the proton flux scaled to the Earth orbit $(n_p U_p)_{\mathrm{E}}$, (b) the ion flux ratio $(n_\alpha U_\alpha)/(n_p U_p)$, ($c$) the local maximum of the alpha abundance represented by $n_{\alpha p, M}$, (d) the location of the Alfvén point r_A, (e) the proton-alpha differential speed $U_{\alpha p, \mathrm{A}}$ at the Alfvén point, and (f) the loss of the wave energy between 1 and 100 $R_\odot$, denoted by ΔW. Also given are the values at 100 $R_\odot$ for (g), (h), and (i) the proton and alpha speeds, $U_{p,100}$ and $U_{\alpha,100}$, as well as the proton-alpha speed difference $U_{\alpha p,100}$. Let us consider Figures 4a–4e first. One can see that as far as the wave effects inside the Alfvén point are concerned, for $\omega \gtrsim 3.5 \times 10^{-3}$ rad s^{-1}, the relative difference of the computed parameters with respect to the WKB values is less than 10%. In other words, the WKB limit provides an adequate description for these high-frequency waves. However, for lower frequencies significant differences tend to appear between the non-WKB and WKB models, with the latter being always more effective in accelerating the solar wind, as indicated by the smaller r_A (see Fig. 4d). On the other hand, Figure 4b indicates that the difference between the WKB and non-WKB values for the ion flux ratio is rather modest; even for $\delta u_b = 40$ km s^{-1} the relative difference is $\lesssim 10.2\%$. Given that the proton flux is substantially enhanced in the WKB case (see Fig. 4a), this modest difference in the ion flux ratio means that relative to the non-WKB waves, the WKB ones boost the fluxes of both ion species to nearly equal extent. Note that this does not guarantee that the alpha abundance in the inner corona is only slightly modified by the non-WKB effect. In fact, the local maximum $n_{\alpha p, M}$, which varies from 0.168 to 0.182 for $4 \times 10^{-5} \leq \omega \leq 2 \times 10^{-3}$ rad s^{-1} in the series where $\delta u_b = 40$ km s^{-1}, is up to 77.3% larger than $n_{\alpha p, M} = 0.102$ obtained in the WKB model. As for the proton-alpha speed difference, Figure 4e shows that the waves with $\delta u_b \gtrsim 16$ km s^{-1} have appreciable effect in limiting its magnitude already inside the Alfvén point. Moreover, the wave with $\omega = 8 \times 10^{-4}$ rad s^{-1} seems to be the most inefficient in achieving this effect in each series. Now consider Figures 4f to 4i, where the wave effects on the asymptotic flow parameters are examined. It can seen in Figure 4f that in general the asymptotic proton speed U_p is correlated with the wave energy loss ΔW, a consequence of relation (17). However, the correlation disappears for the lowest wave amplitude in the segment $\omega \lesssim 5 \times 10^{-5}$ rad s^{-1}. This is not
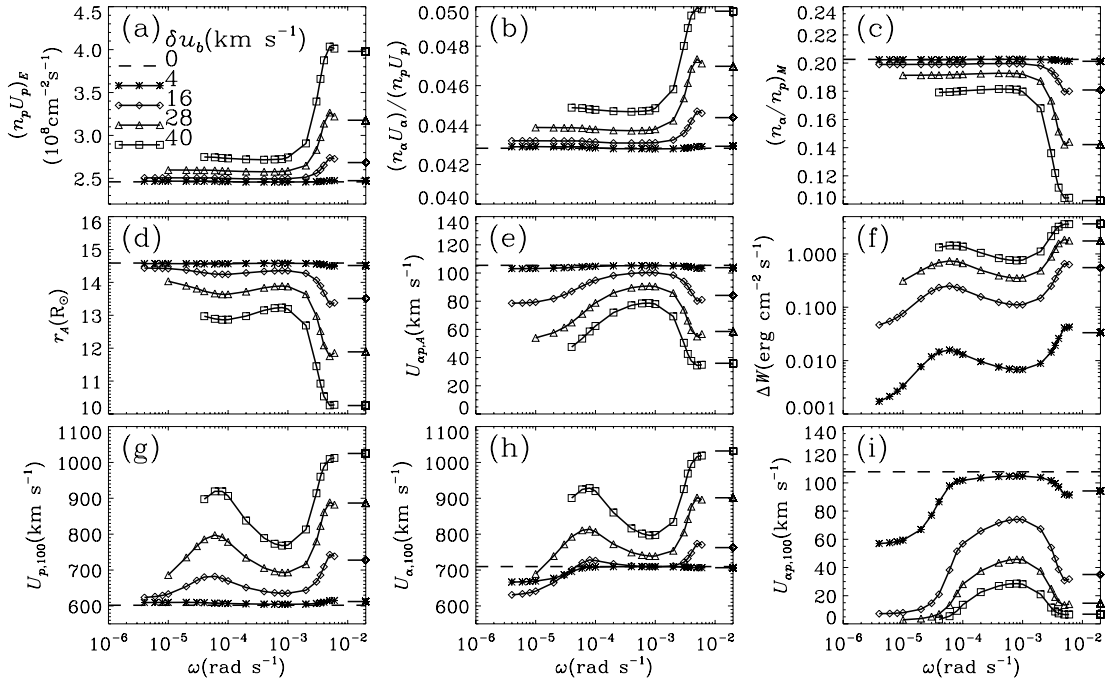
Fig. 4.—Frequency dependence of several parameters characterizing the multicomponent solar wind solutions self-consistently incorporating non-WKB Alfvén waves. The four series of models pertain to different base velocity fluctuation amplitudes, as indicated in (a). In addition, the dashed lines give the waveless model, i.e., $\delta u_b = 0$. (a) The proton flux scaled to the Earth orbit, $(n_p U_p)_E$. (b) The ratio of the alpha flux to the proton flux, $(n_\alpha U_\alpha)/(n_p U_p)$. (c) The local maximum in the inner corona of the alpha abundance, $(n_\alpha/n_p)_M$. (d) The location of the Alfvén point, r_A. (e) The proton-alpha speed difference at the Alfvén point, $U_{\alpha p, A}$. (f) The difference of W, the wave energy flux density scaled to the Earth orbit, between 1 and 100 $R_\odot$. (g), (h), and (i) The proton $U_{p,100}$ and alpha $U_{\alpha,100}$ flow speeds, as well the proton-alpha speed difference $U_{\alpha p,100}$ at 100 $R_\odot$. For comparison, the parameters derived in the corresponding WKB wind models are given by the short horizontal bars in each panel.

surprising, since in this case the wave energy loss ΔW is too low to play a role. As a matter of fact, in this frequency range ΔW is $\lesssim 0.93\%$ of F_E, the energy flux associated with the ion heating. However, despite this, the waves show appreciable effects in limiting the proton-alpha speed difference (see Fig. 4i). Specifically, in the waveless model, $U_{\alpha p,100} = 108$ km s^{-1}, whereas in the model with $\omega = 10^{-5}$ rad s^{-1}, $U_{\alpha p,100}$ is 59.4 km s^{-1}. The reduction is seen to be achieved by a reduction in U_α and an increase in U_p (Figs. 4g and 4h). Comparing Figure 4i with 4e, one can see that between r_A and 100 $R_\odot$, $U_{\alpha p}$ is further reduced. Furthermore, the feature that the waves with $\omega = 8 \times 10^{-4}$ rad s^{-1} correspond to the largest $U_{\alpha p}$ for a given series also shows up in Figure 4i. At the higher and lower ends of the frequency range, $U_{\alpha p,100}$ nearly vanishes for wave amplitudes $\delta u_b \gtrsim 16$ km s^{-1}.

4.2. Slow Solar Wind Solutions

Let us now move on to discuss the slow solar wind, or rather, how Alfvén waves may influence the flow parameters in models obtained along tube S indicated in Figure 1 using the heating and boundary flow parameters corresponding to "slow wind" in Table 1. For the chosen parameters, the waveless model yields a proton flux of $(n_p U_p)_E$ of 3.73×10^8 cm^2 s^{-1} and an ion flux ratio of $(n_\alpha U_\alpha)/(n_p U_p) = 0.04$. A local maximum of the alpha abundance $n_{\alpha p, M} = 0.185$ is found at 1.9 $R_\odot$. The flow reaches the Alfvén point at 17.2 $R_\odot$, where the proton (alpha) speed is 258 (367) km s^{-1}, the resulting speed difference being 109 km s^{-1}. At 100 $R_\odot$, $U_p = 290$ km s^{-1} and $U_\alpha = 370$ km s^{-1}. It is noteworthy that the corresponding $U_{\alpha p} = 80$ km s^{-1} is not unrealistic for slow solar winds, even larger values have been found by *Helios 2* when approaching perihelion (Marsch et al. 1981).

Figure 5 presents, in the same format as Figure 4, the frequency dependence of several flow parameters obtained in four series of solar wind models with different δu_b. In addition, the WKB and

waveless models are also given. A comparison with Figure 4 indicates that nearly all the features in Figure 5 are reminiscent of those obtained for fast solar wind solutions. In particular, Figures 5a and 5d indicate that the non-WKB waves produce a proton flux up to 32.3% lower, a value for the location of the Alfvén point up to 31.2% higher than their WKB counterparts. As in the case of fast wind solutions, the WKB and non-WKB Alfvén waves show only a modest difference in the derived ion flux ratio, indicating that the larger wave accelerations in the WKB case boost the fluxes of both species to similar degrees (see Fig. 5b). However, for the local maximum alpha abundance $n_{\alpha p, M}$ in the inner corona, the non-WKB values may be up to 91.5% larger (Fig. 5c). Furthermore, Figure 5e indicates that for $\delta u_b \gtrsim 16$ km s^{-1}, both WKB and non-WKB waves may substantially reduce $U_{\alpha p}$ inside r_A. Note that the waves with $\omega \sim 2 \times 10^{-4}$ rad s^{-1} are the most inefficient in achieving this effect, and the same feature persists in Figure 5i, which shows that $U_{\alpha p}$ at 100 $R_\odot$ is no larger than 27.9 km s^{-1} for all models with $\delta u_b \gtrsim 16$ km s^{-1}. Interestingly, at this distance, the waves with the lowest frequency may also be effective even with the lowest amplitude. In fact, for $\omega = 8 \times 10^{-6}$ rad s^{-1}, the waves with $\delta u_b = 4$ km s^{-1} yield $U_{\alpha p,100} = 24.6$ km s^{-1}, even though the corresponding wave energy loss is merely 0.013 erg cm^{-2} s^{-1}, amounting to 1.1% of the empirical energy flux exhausted to heat ion fluids (cf. Fig. 5f). In this particular case, the wave energy flux plays no part in the solar wind acceleration; rather, waves provide a net acceleration for the protons but a net deceleration for the alpha particles (cf. Figs. 5g and 5h). Moreover, Figures 5g and 5h indicate that for $\delta u_b = 16$ km s^{-1}, compared with the waveless values U_α for $\omega = 8 \times 10^{-6}$ rad s^{-1} is barely larger, but U_p shows a significant increase, by 95 km s^{-1}. On the other hand, for the WKB and the majority of the non-WKB waves, both U_p and U_α are enhanced relative to the waveless values. This once again reinforces the notion that
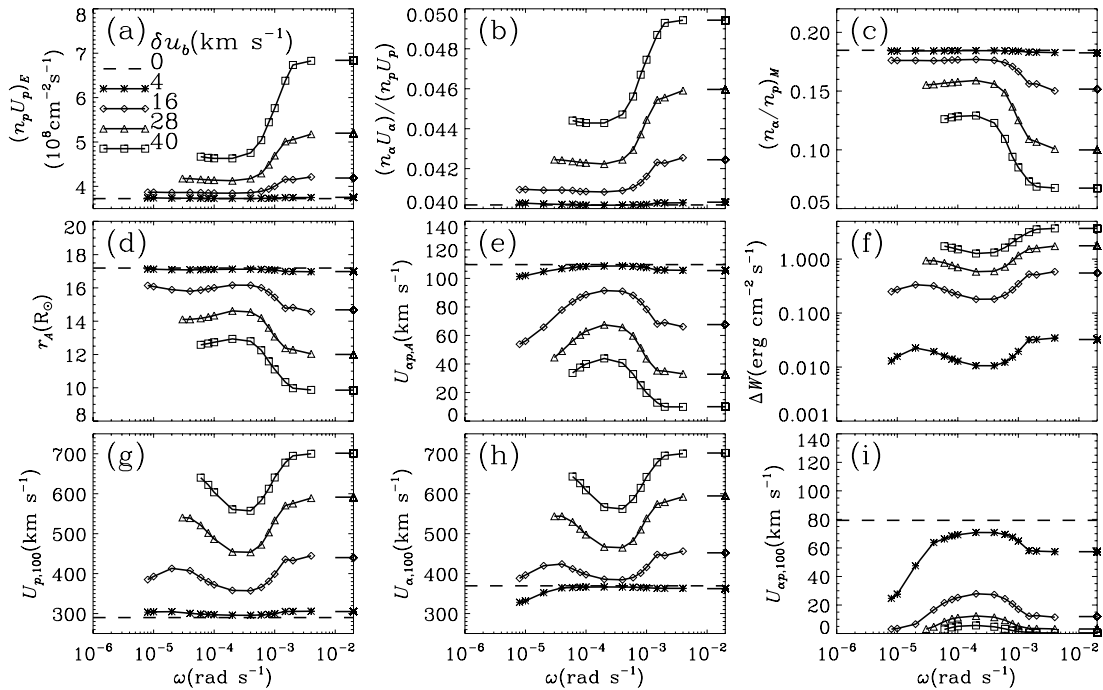
Fig. 5.— Similar to Fig. 4 but for the slow solar wind solutions.

different mechanisms operate at different frequency regimes. A further comparison with Figures 4 indicates that some quantitative differences arise in Figure 5 nonetheless. One can see that the non-WKB values approach the corresponding WKB values at a lower frequency. To be more specific, the WKB limit provides a description with relative differences within 10% for the wave behavior as long as $\omega \gtrsim 1.5 \times 10^{-3}$ rad s^{-1}. This happens in conjunction with the lowering of the critical value ω_c below which the waves behave in a quasi-static rather than a wavelike way. For the solutions examined, a value of 1.3×10^{-5} rad s^{-1} may be quoted for ω_c.

5. SUMMARY AND CONCLUDING REMARKS

This study has been motivated by the observational facts that Alfvénic fluctuations exist in both fast and slow solar winds (Marsch et al. 1981, 1982a, 1982b), and for the majority of the measured fluctuations the corresponding frequency is too low to allow the short-wavelength WKB limit to apply (e.g., Tu & Marsch 1995). Specifically, using the formulation given in Li & Li (2007) we have constructed multicomponent solar wind models that treat protons and alpha particles on an equal footing and that self-consistently incorporate the contribution from dissipationless, monochromatic, hydromagnetic (with angular frequencies ω well below ion gyrofrequencies), toroidal Alfvén waves. The waves, which smoothly pass the Alfvén point where the combined meridional Alfvénic Mach number M_T equals 1 (cf. eq. [6]), are coupled to the flow solely through the wave-induced ponderomotive forces. Azimuthal symmetry about the magnetic axis is assumed throughout, and solar rotation is neglected. However, no assumption has been made that the wavelength is small compared to the spatial scales at which the solar wind parameters vary. Starting with a waveless model, for the fast and slow solar wind alike, we obtained a grid of models corresponding to different ω and base wave amplitudes δu_b, defined as the amplitude of the electron velocity perturbation $\langle u_e^2 \rangle^{1/2}$ at 1 $R_\odot$. The non-WKB effect is then examined, in a systematic and quantitative fashion, by comparing the models with that incorporating WKB waves

with the same δu_b, as shown by Figures 4 and 5. The results can be summarized as follows:

1. The non-WKB effects are significant for the majority of the examined solutions. In comparison with comparable WKB waves, the non-WKB waves are less effective in accelerating the solar wind inside the Alfvén point. As a consequence, non-WKB Alfvén waves may produce a proton flux up to 32% lower, and an Alfvén point 29% farther from the Sun than their WKB counterparts for fast solar wind solutions. Even though the ion flux ratio increases by $\lesssim$10% from non-WKB to WKB models, indicating that the WKB waves boost the fluxes of both ion species to a similar extent, the maximum of the alpha abundance, $n_{\alpha p,M}$, is considerably affected by the non-WKB effect, with the non-WKB values being up to 77% higher than the WKB ones. The differences between WKB and non-WKB models are more prominent for slow solar wind solutions, for which the non-WKB models produce values for $n_{\alpha p,M}$ up to 92% higher. It is also found that the influence associated with non-WKB effects tends to decrease with increasing frequency: the waves in the fast (slow) winds with $\omega \gtrsim 3.5 \times 10^{-3}$ (1.5×10^{-3}) rad s^{-1} can be described by the WKB limit with an accuracy to better than 10%.

2. While the Alfvén waves tend to reduce the magnitude of the proton-alpha speed difference $|U_{\alpha p}|$ in general, different mechanisms operate in two different regimes, separated by a critical frequency ω_c, which in principle may be different from model to model especially when the wave base amplitude δu_b is large. For the range in which δu_b is varied in the examined numerical solutions, however, ω_c hardly varies with δu_b and is found to be $\sim 3 \times 10^{-5}$ ($\sim 1.3 \times 10^{-5}$) rad s^{-1} for the fast (slow) solar wind models. When $\omega > \omega_c$, the fluctuations are wavelike and tend to accelerate both ion species, thereby losing most of their energy in doing work on ion flows. On the other hand, when $\omega < \omega_c$, a quasi-static behavior results: the fluctuations may act to accelerate the slower flowing ion species but decelerate the faster moving one in a large portion of the computational domain, and only a minor fraction of the wave energy flux injected at the base is lost. The fluctuations with the lowest frequency are no less

efficient in reducing $|U_{\alpha p}|$ than the WKB waves; in the slow solar wind solutions, they may be able to quench a significant $|U_{\alpha p}|$ with base amplitudes as small as 4 km s^{-1}.

Before proceeding, we note that to examine the wave effects on the solar wind, an alternative approach would be to directly solve the multifluid equations, where the Alfvén waves are introduced via boundary conditions (cf. Ofman 2004). In our study, monochromatic waves are invoked, so that a detailed understanding of the frequency dependence of the solar wind properties may be found. On the other hand, Ofman (2004) introduced a broad spectrum of Alfvén waves into a resistive and viscous solar wind plasma. Consequently, a comparison of his model with ours is not straightforward. Nevertheless, in a previous study (Ofman & Davila 1998), where monochromatic Alfvén waves were used and a set of isothermal single-fluid MHD equations were solved, the authors concluded that their results agree with the studies of a single-fluid isothermal wind as conducted by MacGregor & Charbonneau (1994), who used essentially the same approach as ours. From this, we may conclude that the results obtained in this paper may well be supported by direct numerical solutions, the construction of which will be presented in a future publication.

Another way to extend the current model is to use a spectrum of Alfvén waves instead of monochromatic ones. This would also be more consistent with observations which show that in reality, the Alfvénic fluctuations span a broad spectrum and do not possess a preferred frequency (e.g., Tu & Marsch 1995). With this caveat in mind, the presented study nonetheless provides a better understanding of the underlying physics. For instance, when a spectrum is taken into account, one may expect that net effect will also be that the magnitude of the proton-alpha speed difference is reduced, and the reduction will have some dependence on the spectral slope. In addition, the existence of an ω_c of the order of several times 10^{-5} rad s^{-1} may have significant consequences for the spectrum of the velocity perturbations of alpha particles, denoted by P_α for brevity. In the present study we have concentrated on monochromatic waves for the purpose of presenting a systematic study of the effects brought forth by the finite wavelength. However, from the results obtained in the present paper and Paper I (Li & Li 2007), it is possible to deduce some properties of P_α in the presence of transverse Alfvénic fluctuations. From an observational point of view, the spectrum of proton velocity fluctuations, P_p, has been less extensively studied than that of the magnetic field fluctuations, P_B, because of the considerably lower temporal resolution of plasma instruments relative to magnetometers (cf. Podesta et al. 2006, 2007). Measuring P_α is even more difficult given that the alpha particles are more tenuous. As a result, such a study of P_α has yet to appear, but is certainly feasible for plasma instruments on board future missions such as the *Solar Orbiter* or *Solar Probe*. This is because these missions may approach the Sun as close as 4 $R_\odot$, where the alpha particles to be sampled will be much hotter and have a much larger number density than in the near-Earth regions.

Let us now picture what P_α in fast solar winds may look like in the super-Alfvénic regions (beyond, say, $\sim$40 $R_\odot$, where the Alfvénic Mach number $M_T \gtrsim 3$), supposing that the waves are propagating parallel to a radial magnetic field, and that $U_{\alpha p} = U_A$, $x_\alpha = 0.2$, and $x_p = 0.8$, where $x_k = \rho_k/\rho$ ($k = p, \alpha$). For frequencies corresponding to $\omega > \omega_c$, the fluctuations are genuinely wavelike, and one expects that a WKB behavior will result.

It then follows from equations (25) and (41) in Paper I that the ratio of the amplitude of alpha to proton velocity perturbations

$$\eta \approx \frac{1 - x_p - x_p x_\alpha/2}{2 - x_p - x_p x_\alpha/2} \approx 0.11.$$

On the other hand, for $\omega < \omega_c$, a quasi-static manner results, and an analogy is readily drawn with the problem of angular momentum transport in a multicomponent solar wind. In this case, equations (2a) and (2b) in Li et al. (2007), which are equivalent to the zero-frequency limit treated in Paper I, are more convenient to use and yield $\eta \approx (\rho_p U_p)/(\rho_\alpha U_\alpha) \gtrsim 3$ by noting that the amplitudes are largely determined by the terms associated with $U_{\alpha p}$. Consequently, in the spectrum of the velocity fluctuations of alpha particles P_α, one may see an apparent spectral break at ω_c, around which the spectrum shows a steep slope provided that the proton velocity fluctuation spectrum is somehow smooth here. Whether $P_\alpha(\omega)$ behaves like this in reality remains to be tested by future in situ measurements.

REFERENCES

Alazraki, G., & Couturier, P. 1971, A&A, 13, 380
Banaszkiewicz, M., Axford, W. I., & McKenzie, J. F. 1998, A&A, 337, 940
Banerjee, D., Teriaca, L., Doyle, J. G., & Wilhelm, K. 1998, A&A, 339, 208
Belcher, J. W., & L. Davis, Jr. 1971, J. Geophys. Res., 76, 3534
Bruno, R., & Carbone, V. 2005, Living Rev. Sol. Phys., 2, 4, http://www.livingreviews.org/lrsp-2005-4
Chae, J., Schühle, U., & Lemaire, P. 1998, ApJ, 505, 957
Cranmer, S. R., & van Ballegooijen, A. A. 2005, ApJS, 156, 265
Cranmer, S. R., van Ballegooijen, A. A., & Edgar, R. J. 2007, ApJS, 171, 520
Delaboudinière, J. P. 1999, Sol. Phys., 188, 259
Dmitruk, P., Milano, L. J., & Matthaeus, W. H. 2001, ApJ, 548, 482
Esser, R., Fineschi, S., Dobrzycka, D., et al. 1999, ApJ, 510, L63
Gary, S. P., Yin, L., Winske, D., & Reisenfeld, D. B. 2000, Geophys. Res. Lett., 27, 1355
Goldstein, M. L., Roberts, D. A., & Matthaeus, W. H. 1986, J. Geophys. Res., 91, 13357
———. 1995, ARA&A, 33, 283
Hansteen, V. H., Leer, E., & Holzer, T. E. 1997, ApJ, 482, 498
Heinemann, M., & Olbert, S. 1980, J. Geophys. Res., 85, 1311
Hollweg, J. V. 1973, J. Geophys. Res., 78, 3643
Hollweg, J. V., Bird, M. K., Volland, H., et al. 1982, J. Geophys. Res., 87, 1

Hollweg, J. V., & Isenberg, P. A. 2002, J. Geophys. Res., 107(A7), DOI: 10.1029/2001JA000270
———. 2007, J. Geophys. Res., 112, A08102, DOI: 10.1029/2007JA012253
Holzer, T. E., & Axford, W. I. 1970, ARA&A, 8, 31
Hu, Y. Q., Esser, R., & Habbal, S. R. 1997, J. Geophys. Res., 102, 14661
Hu, Y. Q., & Habbal, S. R. 1999, J. Geophys. Res., 104, 17045
Isenberg, P. A., & Hollweg, J. V. 1983, J. Geophys. Res., 88, 3923
Laming, J. M., & Feldman, U. 2003, ApJ, 591, 1257
Li, B., Habbal, S. R., & Li, X. 2007, ApJ, 661, 593
Li, B., & Li, X. 2006, A&A, 456, 359
———. 2007, ApJ, 661, 1222 (Paper I)
Li, X. 2003, A&A, 406, 345
Lie-Svendsen, Ø., Hansteen, V. H., & Leer, E. 2003, ApJ, 596, 621
Lou, Y.-Q. 1993, J. Geophys. Res., 98, 3563
MacGregor, K. B., & Charbonneau, P. 1994, ApJ, 430, 387
Marsch, E., Mühlhäuser, K.-H., Rosenbauer, H., Schwenn, R., & Denskat, K. U. 1981, J. Geophys. Res., 86, 9199
Marsch, E., Mühlhäuser, K.-H., Rosenbauer, H., Schwenn, R., & Neubauer, F. M. 1982a, J. Geophys. Res., 87, 35
Marsch, E., Mühlhäuser, K.-H., Schwenn, R., Rosenbauer, H., Pilipp, W., & Neubauer, F. M. 1982b, J. Geophys. Res., 87, 52

McComas, D. J., Barraclough, B. L., Funsten, H. O., et al. 2000, J. Geophys. Res., 105, 10419

McKenzie, J. F., Ip, W.-H., & Axford, W. I. 1979, Ap&SS, 64, 183

Ofman, L. 2004, J. Geophys. Res. A, 109, A07102, DOI: 10.1029/2003JA010221

Ofman, L., & Davila, J. M. 1998, J. Geophys. Res., 103, 23677

Parker, E. N. 1965, Space Sci. Rev., 4, 666

Peter, H. 1999, ApJ, 516, 490

Podesta, J. J., Roberts, D. A., & Goldstein, M. L. 2006, J. Geophys. Res. A, 111, A10109, DOI: 10.1029/2006JA011834

———. 2007, ApJ, 664, 543

Smith, E. J., & Balogh, A. 1995, Geophys. Res. Lett., 22, 3317

Spitzer, L. Jr. 1962, Physics of Fully Ionized Gases (New York: Wiley)

Tu, C.-Y., & Marsch, E. 1995, Space Sci. Rev., 73, 1

Velli, M. 1993, A&A, 270, 304

Verdini, A., & Velli, M. 2007, ApJ, 662, 669

Verdini, A., Velli, M., & Oughton, S. 2005, A&A, 444, 233

Verheest, F. 1977, Ap&SS, 46, 165

Zhou, Y., & Matthaeus, W. H. 1990, J. Geophys. Res., 95, 10291